

Sestito J.M. , Liu D., Lu Y., Song J.-H., Tran A.V., Kempner M.J., Harris T.A.L., Ahn S.-H., and Wang Y. (2021) Multiscale process modeling of shape memory alloy fabrication with directed energy deposition. *Manufacturing in the Era of 4th Industrial Revolution - Vol. 1. Recent Advances in Additive Manufacturing*, eds. by H. Bruck, Y. Chen, and S.K. Gupta (World Scientific), Ch.3, pp. 41-76.

Chapter 3

Multiscale Process Modeling of Shape Memory Alloy Fabrication with Directed Energy Deposition

Jesse M. Sestito[†], Dehao Liu[†], Yanglong Lu[†], Ji-Hyeon Song^{†‡}, Anh V. Tran[†], Michael J. Kempner[†], Tequila A. L. Harris[†], Sung-Hoon Ahn[‡], and Yan Wang^{†*}

[†]Georgia Institute of Technology, Atlanta, USA

[‡]Seoul National University, Seoul, South Korea

*Correspondence: Tel: +1-404-894-4714. Email: yan.wang@me.gatech.edu

1.1 Introduction

A shape memory alloy (SMA) is a functional material which can return to its pre-deformed shape when experiencing external thermal or mechanical loads. This so-called shape memory effect is caused by the solid-state phase transition between the martensitic and austenitic phases. SMAs also display pseudoelasticity or superelasticity, which is characterized by a reversible stress-strain behavior with higher strain values than classic alloys. These unique properties make SMAs attractive for applications such as medical implants, stents, actuators, sensors, foldable devices, among others [1, 2]. Copper zinc aluminum (CuZnAl), copper aluminum nickel (CuAlNi), and Nitinol (NiTi) are the three most studied SMAs and are commercially available. Particularly, Nitinol, which is a blend of nickel and titanium, is the most commonly used one because of its stability and biocompatibility [3].

In spite of its great potential for new product concepts, several challenges exist in the fabrication of SMAs in traditional manufacturing methods such as casting and rolling, including difficulty of controlling material impurities, localized concentrations of materials for specific applications, fine tuning mechanical properties, as well as eliminating or introducing porosity in the structures [4, 5]. In recent years, researchers have examined the properties of SMAs made by additive manufacturing (AM) techniques. AM overcomes some of these challenges and potentially allows engineers to customize the structures and control the localized compositions and processing temperatures for SMAs.

Metallic AM techniques such as selective laser melting (SLM) and directed energy deposition (DED) have been applied to fabricate SMAs. Researchers investigated the impact of AM process parameters on the properties of Nitinol by tweaking the process parameters [6, 7], varying material concentration [6], and exploring various porosities for biomedical applications [8]. There is also research being performed to exam the structural integrity of Nitinol [1] and the impacts of porosity on the material properties [9]. Despite the knowledge elicited by these studies, there is still a lack of fundamental understanding of the AM processes and their influence on the physical properties of SMAs. Systematically exploring the process-structure-property (P-S-P) relationships and understanding the microstructure formation in complex AM processes will be necessary for us to design, optimize, and control these processes. Tools developed for integrated computational materials engineering (ICME) can be helpful in materials and process design.

The P-S-P relationships for SMAs made by AM are very complex with many different factors involved. For instance, different biomedical implants of Nitinol require different levels of porosity, depending on the specific requirements of local transport and mechanical properties. The abundant combination of process parameters such as laser power, scanning strategy, and layer thickness can produce a variety of Nitinol alloys with SLM or DED. Different compositions of Ni, Ti, and dopants can alter the growth of grain structures during solidification, as well as the dynamic behaviors of shape change and phase transition with different characteristics of hysteresis. Simply relying on physical experiments to test different combinations of all process and material factors to explore the P-S-P relationships is prohibitively expensive and not feasible for process and materials design. Simulation is an efficient alternative to facilitate the design and optimization process.

Researchers have used simulations to study SMAs. For instance, molecular dynamic simulations have been used to study the melting curve of Nitinol under pressure [10] and examine the transformation mechanical properties under the presence of Ni_4Ti_3 precipitates [11]. Phase field simulations have been used to examine the addition of free surfaces and boundary condition changes to the material [12] and the impact of thermal cycling on the plasticity [13]. Finite element simulations have been used to examine properties of Nitinol composite beam [14] and multiaxial loading on the SMA [15]. Kinetic Monte Carlo simulations have been used to study the magnetic behavior and its dependence on static temperature [16] and variable temperature [17]. These simulation models were developed to understand the structure-property relationship of SMAs. To establish the complete P-S-P relationships and facilitate the design of AM processes for SMAs, a multiscale modeling and simulation approach is needed. To understand the effects of material compositions on detailed microstructures and physical properties, atomistic simulations are necessary. However, atomistic simulations are only capable of simulating processes with very short time scales

(e.g. nanosecond or less) and cannot simulate manufacturing processes in order to construct process-structure relationships.

In this chapter, a multiscale multi-physics simulation framework is described to help establish the P-S-P relationships for SMAs processed with AM. The simulation framework includes finite element analysis (FEA) to predict thermal and multiphase flow phenomena in AM processes, controlled kinetic Monte Carlo (cKMC) as a reduced-order AM process simulation model for porosity and morphology predictions, phase field method (PFM) coupled with thermal lattice Boltzmann method (TLBM) to simulate the solidification of SMAs and understand the effects of process parameters and material compositions on grain formation, as well as molecular dynamics (MD) to predict thermal, transport, and mechanical properties that are used as the inputs of FEA, cKMC, PFM, and TLBM simulations. The proposed multiscale process modeling and simulation framework is shown in Figure 1. Here, the generic framework is illustrated with the DED process to fabricate Nitinol.

The remainder of this chapter is organized as follows. In Section 1.2, MD simulations to predict material properties of Nitinol are demonstrated. Structure-property relationships such as the effects of material compositions on melting temperature, thermal conductivity, viscosity, and other physical properties are predicted. This allows for materials design to choose appropriate compositions. The predicted properties are also necessary input parameters for simulations at larger scales. In Section 1.3, multi-physics PFM and TLBM are demonstrated with the elucidation of the detailed solidification process at mesoscale. The effect of grain growth pattern and final crystallographic texture on the compositions of Ni and Ti, melt pool flow, cooling rate, and other process parameters are shown. In Section 1.4, the continuum level multi-physics FEA simulation predicts the temperature and velocity fields in the melt pool so that the details of the melting process can be revealed. The evolutions of temperature and velocity fields are also important input parameters for PFM and TLBM simulations at mesoscale. In Section 1.5, a cKMC model to simulate the DED process at the system level is demonstrated, where porosity and microscopic morphology can be predicted at a much lower cost than FEA. This reduced-order model is an efficient alternative for system-level simulation for path planning and large-scale process optimization.

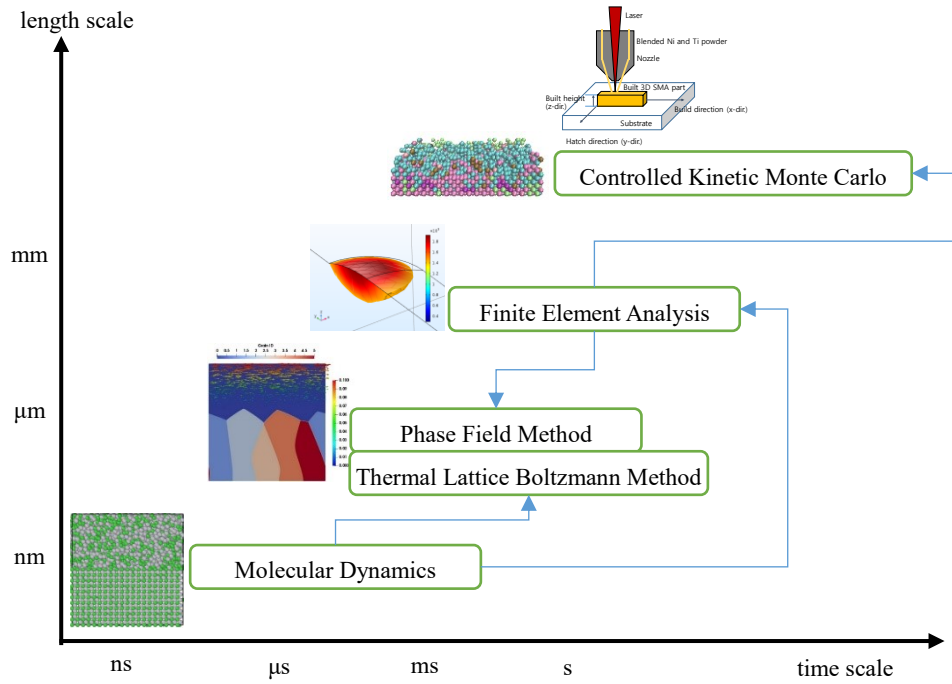


Figure 1. The multiscale multiphysics simulation framework to explore process-structure-property relationship for additively manufactured shape memory alloys

1.2 Property Calculation with MD Simulations

MD is a simulation method focused on the dynamics of individual particles in a material system, where each particle is an atom or a group of atoms. During simulation, each particle interacts with nearby particles, which is characterized by inter-atomic potential functions depending on particle positions. Inter-atomic potentials determine the inter-atomic forces. The dynamics of particles is simulated with continuous update of the positions and velocities of all particles at each time step. These time steps are normally on the order of femtoseconds. In addition, a few million atoms can only fill out a cube of one hundred nanometers. Therefore, most MD simulations predict material systems at the nanometer scale for only a period of nanoseconds. MD is not optimal for simulating processes such as melting and solidification of the crystalline structures at the micrometer and second scales. Instead, MD simulations are employed to gain an understanding of how atomic movement dictates material properties.

In the following subsections, it will be shown that using MD one can calculate properties of Nitinol. Not only will these properties be useful for gaining insight of the material's structure-property relationship, but they are necessary

inputs of other simulation methods such as PFM, FEA, and cKMC to obtain more accurate results if there is a lack of experimental data to perform model calibration empirically.

Here, MD will be used to estimate the melting temperature of Nitinol. The compositions of Ni, Ti, and other elements in Nitinol can be tailored for specific device design with targeted phase transition behavior, because their melting temperature could be different. Melting temperature is an important parameter to consider in designing AM processes. Therefore, MD calculation of melting temperature is useful for materials design and process design. Similarly, thermal conductivity is an important material property to design manufacturing processes. The Green-Kubo method was used in MD simulations to calculate the lattice thermal conductivity of Nitinol 55 and 60. MD simulations can be applied to calculate many other material properties, such as dynamic viscosity, anisotropy, interfacial energy, and interface mobility.

1.2.1 Simulation Setup

MD simulations are performed via Large-scale Atomic/Molecular Massively Parallel Simulator (LAMMPS) using a body-centered cubic (BCC) crystal with a lattice constant of 3.512 Angstroms, subject to triaxially periodic boundary conditions. An established second nearest-neighbor (2NN) modified embedded-atom method (MEAM) potential for Nitinol is chosen for its consideration of the directional bonds characteristic of martensitic Nitinol and its ability to relax the material to its empirically observed lattice spacing. The 2NN MEAM potential is a more locally inclusive variation of the classical first nearest-neighbor MEAM potential, which in turn is a version of the traditional embedded-atom model (EAM) potential that has been updated to account for angular forces. Similar to the EAM potential, the 2NN MEAM potential relies on an embedding-energy and a short-range pair potential to describe molecular cohesion within metals. As an MEAM potential, the 2NN MEAM potential is further able to replicate shearing behavior. This allows for a single potential to be used for multiple crystalline configurations, including BCC and face-centered cubic (FCC), enabling simulations of phase changes such as the martensitic-austenitic shift observed in Nitinol. The extension of the potential to consider 2NN interactions corrects for the inadequately reproduced BCC surface energies that have been noted in simulations that neglect the influence of all but the first nearest-neighbors. Two initial setups are used. One setup consists of 16,000 atoms in a one-to-one atomic ratio between Ni and Ti, such that it has approximately 55.08% Ni by mass. The other setup is formed by random deletion of Ti atoms such that the material has approximately 60.00% Ni by mass and consists of 14,540 atoms.

1.2.2 Melting Temperature Prediction

The melting temperature is calculated using the interface method [18–24]. The melting point is estimated to be the temperature at which a discontinuity of a quantity of interest (QoI) is observed. QoIs, including kinetic energy, potential energy, volume, density, temperature, and pressure are monitored. Constant pressure MD simulations are carried out, and the QoI is averaged out over a period.

The simulation cell is split in two regions at the beginning, according to the z coordinate, as shown in Figure 2. Both regions are equilibrated using isothermal isobaric (NPT) statistical ensemble. The temperature corresponding to two regions are different however. In the lower region with smaller z coordinate values, the temperature varies from 1000 K to 1500 K, with 20 K increments. In the region with larger z coordinate values, the temperature is fixed at 5000K, far above the melting temperature. The equilibration phase is carried for 200 ps, where the pressure is set at zero. Figure 2 shows the two-phase solid-liquid of the simulation cell during the first phase of equilibration.

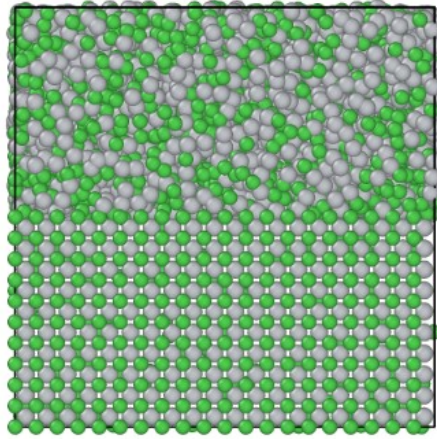


Figure 2. Creation of solid-liquid interface in the molecular dynamics simulation cell.

In the second phase, the simulation cell is reunited, where the NPT ensemble is again applied on the simulated system. The pressure is set to zero, and the temperature varies. The second equilibrium phase is carried out for another 200 ps. The calculation of QoIs is only based on the last 100 ps of the simulation, where the QoIs are averaged with respect to the time.

Presented in Figure 3(a) and (b), respectively, are the ensemble average of the density and mean square displacement for the system with 55.08% of Ni, by the end of the second equilibration phase, as a function of temperature. At about 1400 ± 10 K, a clear discontinuity is observed in both of the monitored QoIs. The density decreases dramatically, and the mean square displacement starts increasing

with the simulated temperature. It is concluded that the melting temperature of Nitinol 55 is 1400 ± 10 K.

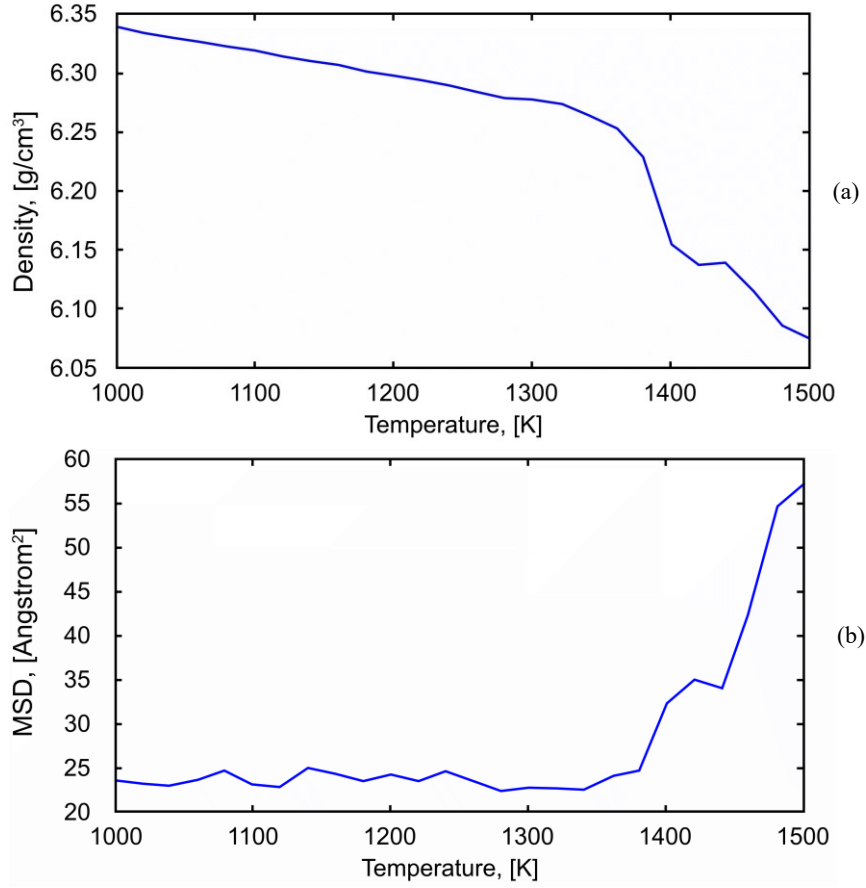


Figure 3. Ensemble averaged density and averaged mean square displacement as functions of the simulated temperature for Nitinol 55.

1.2.3 Thermal Conductivity and Viscosity Prediction

The thermal conductivity, k_m , of a conductor includes the electronic component, k_e , and lattice component, k_g , such that

$$k_m = k_e + k_g \quad (1)$$

is the total thermal conductivity of the material [25]. In MD simulations, the electronic effects can only be indirectly included in the inter-atomic potentials. So for materials with a high electronic component, the calculation of total thermal

conductivity based on MD only could be inaccurate [26]. However, MD does allow the lattice component to be calculated and compared for these materials, such as Nitinol. The electronic thermal conductivity instead can be analytically calculated based on the Wiedemann-Franz law [38, 39] given by,

$$\frac{k_e}{\sigma} = L T \quad (2)$$

where σ is the electric conductivity, T is temperature, and L is the Lorenz number.

With the atomistic setups mentioned in Section 1.2.1, the Green-Kubo method can be applied to predict lattice thermal conductivity [29]. The system is equilibrated at the simulated temperature using a constant pressure and temperature (NPT) ensemble and then constant volume and temperature (NVT) ensemble for 10 ps and 1 ps, respectively. The velocities of atoms are scaled to the simulated temperature prior to the second simulation. This is because the Green-Kubo method requires an equilibrated simulation. The simulation with the NVT ensemble is then run where the average of the auto-correlation of the heat flux is related to thermal conductivity. A 100 ps time average integral value of heat flux auto-correlation gives an estimation of the lattice thermal conductivity. The three calculated lattice thermal conductivities along the x-, y-, and z- axes are shown in Figure 4 (a), where the average of the three is the overall lattice thermal conductivity. These thermal conductivities are calculated from approximately 100 to 1800 K and shown in Figure 4 (b) for 55% and 60% Nitinol using both the MEAM and EAM potentials.

The lattice thermal conductivity results are similar to those of copper-nickel alloys [28]. The lattice thermal conductivity is expected to dissipate at $T^{-0.5}$ [28]. This is shown to be the case in Figure 4 (b). The differences between Nitinol 55 and 60 are also seen. Nitinol 55 has a lower lattice constant than Nitinol 60 in both instances of the EAM and MEAM potentials. With regards to the differences between the MEAM and EAM potentials, at low temperatures the difference is significant, whereas at 400 K and above they produce similar results. Since the focus of the materials in AM processes is for high temperatures, the results of thermal conductivity for temperatures above 1200 K are most important, where both potentials give relatively accurate results.

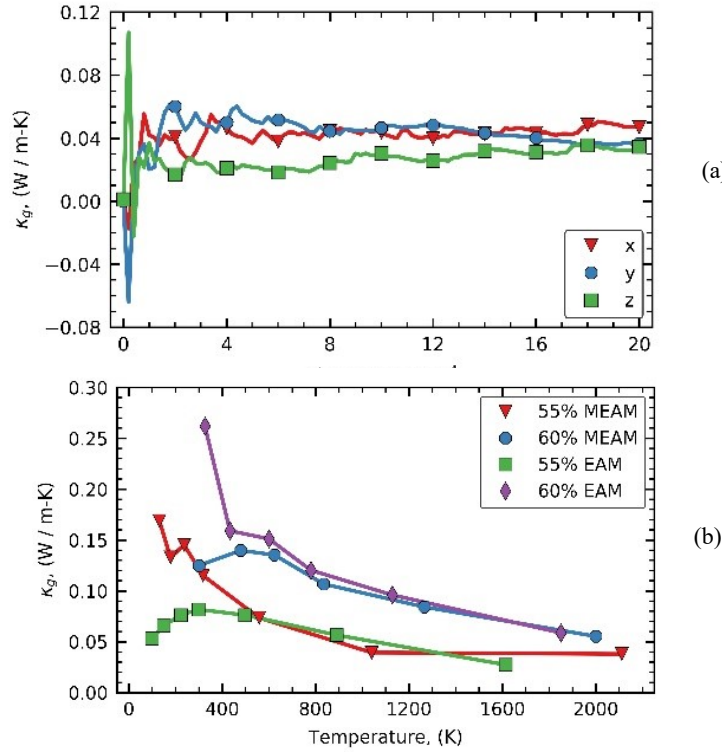


Figure 4. (a) Integration of the auto-correlation heat flux to give the lattice thermal conductivities along the x, y, and z axes over the entire simulation at 1040 K for 55% Nitinol using the MEAM potential. (b) The lattice thermal conductivity with respect to temperature using the MEAM and EAM potentials.

1.3 Solidification Process Simulation with Coupled PFM and TLBM

During the rapid solidification process in DED, solute diffusion, heat transfer, fluid dynamics, as well as their interactions in the melt pool have significant effects on the formation of final solid microstructures. A fundamental understanding of the process allows us to predict the solidified microstructures and the physical properties of the solids for process design and optimization. To understand the solidification of Nitinol alloy, multi-physics simulations at the mesoscale are cost-effective alternatives to expensive experiments for in-situ observation.

Compared to atomistic scale simulations, mesoscale modeling such as PFM [30] is more efficient to simulate the solidification. PFM simulates a much longer time scale than what MD is able to do and provides more fine-grained details than

macroscopic simulations. To distinguish between liquid and solid phases, a continuous variable, namely *phase field* or *order parameter* ϕ , is used in PFM. The evolution of microstructures in solidification is modeled by partial differential equations of phase field, ϕ . In this study, a mesoscale multi-physics model named phase field and thermal lattice Boltzmann method (PF-TLBM) [31, 32] is used to simulate the microstructure evolution of Nitinol during the rapid solidification. In this integrated simulation model, the phase field method for the dendritic growth of a binary alloy is coupled with the thermal lattice Boltzmann method (TLBM) for the heat transfer and melt flow. The detailed formulation of PF-TLBM can be found in Ref. [31, 32].

1.3.1 Simulation Settings

Here, PF-TLBM is used to simulate the directional solidification of Nitinol alloy during the DED process. The physical properties of Nitinol alloy [32–34] are listed in Table 1.

In all simulations, the grid spacing is $\Delta x = 1 \times 10^{-7} \text{ m}$, the time step is $\Delta t = 2 \times 10^{-7} \text{ s}$, and the simulation period is 3 ms. The length and width of the simulated domain are $L_x = 100 \text{ }\mu\text{m}$ and $L_y = 100 \text{ }\mu\text{m}$ in x - and y - directions, respectively. The initial diameter of the seed is $D = 2 \text{ }\mu\text{m}$, and the width of interface is $\eta = 0.5 \text{ }\mu\text{m}$. The setup of boundary conditions for all simulations is schematically illustrated in Figure 5. Zero Neumann conditions are set at the bottom boundary $y = 0$ and top one $y = L_y$ for phase field, ϕ , and composition, C . A fixed heat flux $q_H = \rho c_p L_y \dot{T}$ [36] is set at the bottom boundary given the constant cooling rate $\dot{T} = 5 \times 10^4 \text{ K/s}$, while adiabatic boundary condition is set at the top boundary. When the dendrite grows in a forced flow, a constant flow velocity $|\mathbf{u}_w| = 0.1 \text{ m/s}$ is imposed at the top boundary of the domain. Periodic boundary conditions are set at the left boundary $x = 0$ and right one $x = L_x$ for the phase field (ϕ), composition (C), temperature (T), and flow (\mathbf{u}_l). The nuclei are located at the bottom cold wall with constant heat flux to simulate the directional dendrite growth during DED process. The locations of five nuclei with different orientations are $x = 10 \text{ }\mu\text{m}$, $30 \text{ }\mu\text{m}$, $50 \text{ }\mu\text{m}$, $70 \text{ }\mu\text{m}$, and $90 \text{ }\mu\text{m}$ respectively.

Table 1. Physical properties of Nitinol alloy in the PF-TLBM models

Physical properties	Nitinol 55	Nitinol 60
Liquidus temperature, T_l [K]	1583	1487
Solidus temperature, T_s [K]	1583	1443
Liquidus slope, m_l [K/wt%]	0.0	-19.2
Partition coefficient, k	1.0	0.70
Prefactor of interfacial energy stiffness, σ_0^* [J/m ²]	0.24	0.24
Interfacial energy stiffness anisotropy, ε^*	0.35	0.35
Interface mobility, M_ϕ [m ⁴ /J·s]	1.0×10^{-8}	1.0×10^{-8}
Kinematic viscosity, ν [m ² /s]	8.9×10^{-7}	8.9×10^{-7}
Thermal diffusivity, α [m ² /s]	3.33×10^{-6}	3.33×10^{-6}
Latent heat of fusion, L_H [J/kg·K]	1.0×10^5	1.0×10^5
Specific heat capacity, c_p [J/(kg·K)]	836.8	836.8
Density, ρ [kg/m ³]	6450	6700

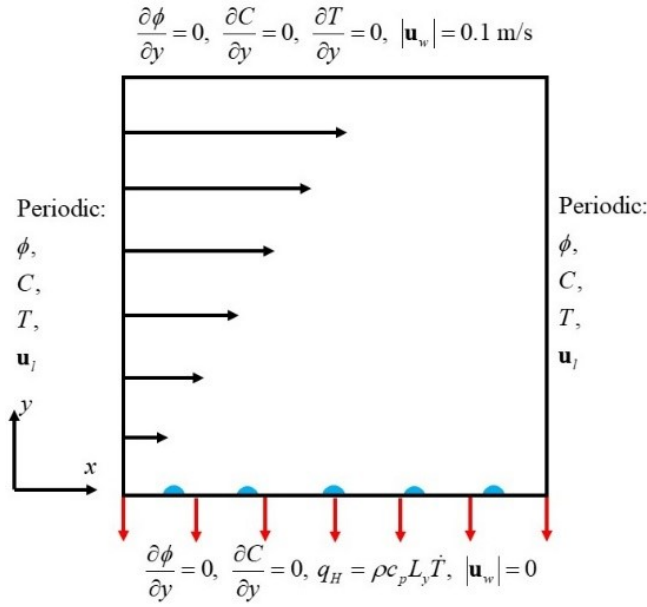


Figure 5. Setup of boundary conditions.

1.3.2 Dendrite Growth of Nitinol 55

The initial concentration of Ni for Nitinol 55 is $C_0 = 55 \text{ wt\%}$ in the liquid phase. It is important to note that the liquidus and solidus temperatures of Nitinol

55 are the same, which means that the solidification of Nitinol 55 is congruent and there is nearly no solute redistribution at the solid-liquid interface during solidification. The initial temperature in the simulation domain is $T = 1580\text{ K}$, which means that the undercooling is 3 K given the initial composition. Figure 6 shows the simulation results. The grain identification (ID) 0 represents the liquid phase, while other grain IDs represent the solid phase with different orientations.

During the congruent solidification of Nitinol 55, there is nearly no solute redistribution at the solid-liquid interface. A cellular growth pattern is observed during the rapid solidification of Nitinol 55, as shown in Figure 6 (a-c). When the grains grow competitively, curved grain boundaries are formed because of different orientations of grains. As shown in Figure 6 (d), the composition of Ni in Nitinol 55 is kept to 55 wt%, and no solute segregation is observed at the grain boundaries. Because of the release of latent heat, the vertical temperature distribution is not monotonic, and the temperature of dendrite tip is higher than liquid melt, as shown in Figure 6 (e).

1.3.3 Dendrite Growth of Nitinol 60

The initial concentration of Ni for Nitinol 60 is $C_0 = 60\text{ wt\%}$ in the liquid phase. The initial temperature in the simulation domain is $T = 1485\text{ K}$, which means that the undercooling is 2 K given the initial composition. The results are shown in Figure 7.

During the congruent solidification of Nitinol 60, solute redistribution occurs at the solid-liquid interface. As shown in Figure 7 (a-b), the cellular growth pattern is observed from 0 to 2 ms. When the solute is ejected from the solid phase to liquid phase, solute segregation is observed at the grain boundaries, where some small portions of liquid are trapped, as shown in Figure 7 (d). Under the influence of solute segregation and released latent heat, the growth velocity of dendrite tip changes significantly. Therefore, the solid-liquid interface is unstable, and consequent transition from a cellular to dendritic microstructure can be observed in Figure 7 (c). Similarly, the vertical temperature distribution is not monotonic, and the temperature of dendrite tip is higher than liquid melt as shown in Figure 7 (e). Because the temperature gradient is along the vertical direction, the vertical secondary arms are dominant in dendrite growth, as shown in Figure 7 (c).

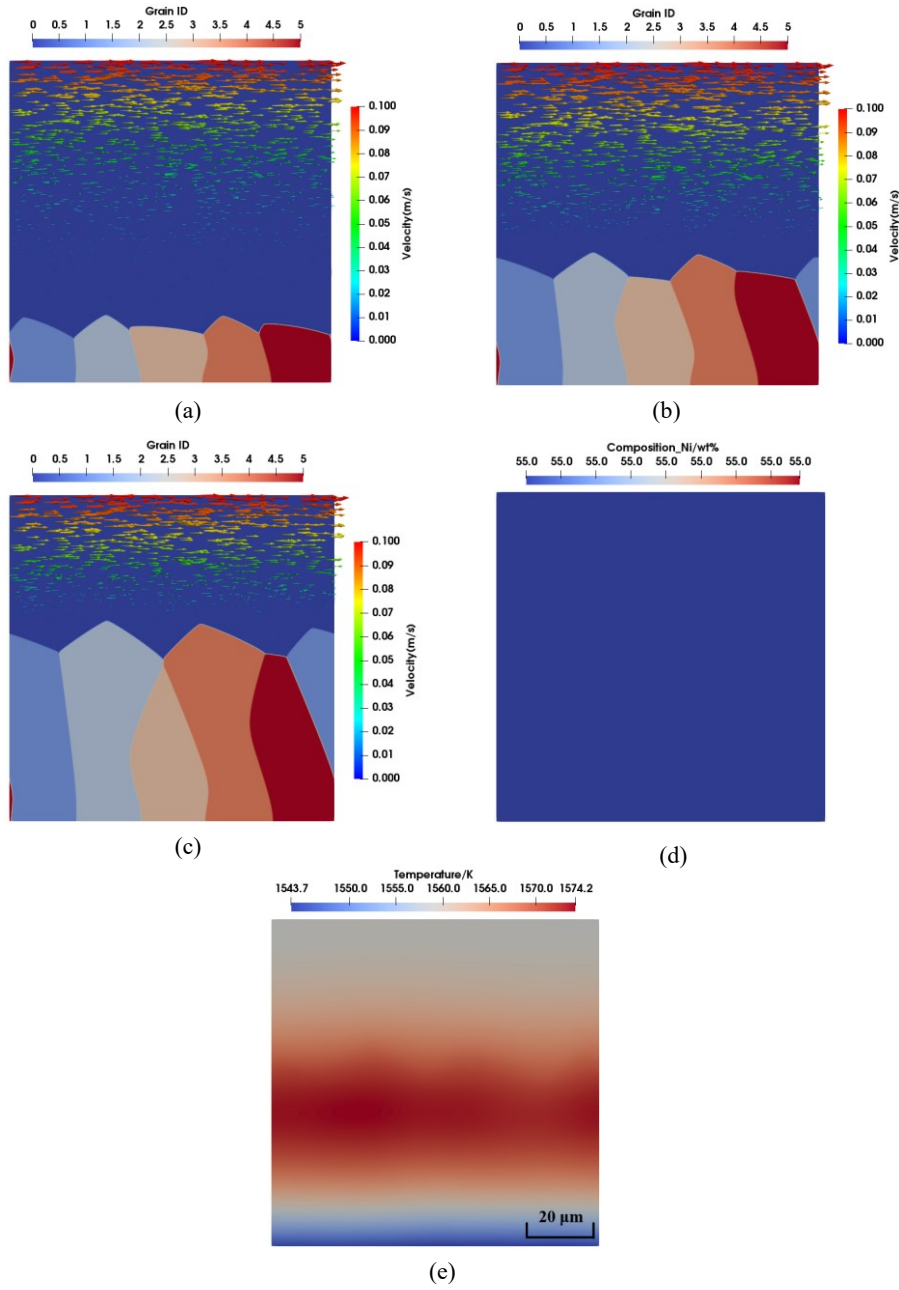


Figure 6. Dendrite growth of Nitinol 55 with latent heat in a forced flow. Phase field and flow field at (a) 1 ms, (b) 2 ms, (c) 3 ms, (d) composition field at 3 ms, and (e) temperature field at 3 ms.

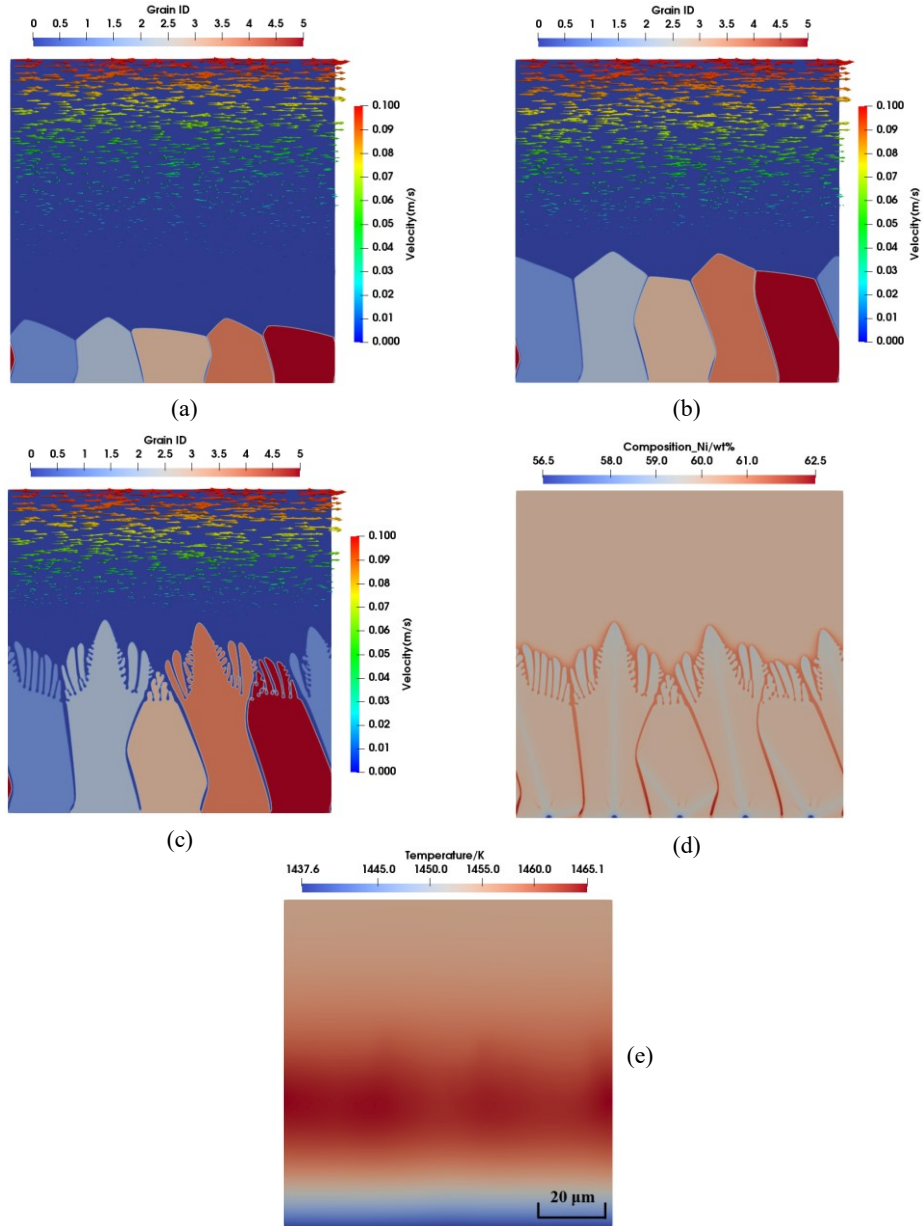


Figure 7. Dendrite growth of Nitinol 60 with latent heat in a forced flow. Phase field and flow field at (a) 1 ms, (b) 2 ms, (c) 3 ms, (d) composition field at 3 ms, and (e) temperature field at 3 ms.

The solute distribution of Ni in Nitinol 55 and Nitinol 60 at the location $y = 10 \mu\text{m}$ at 3 ms are shown in Figure 8. It is observed that the composition of Nitinol 55 keeps 55 wt% along the line, whereas an obvious solute segregation is observed at the grain boundaries of Nitinol 60. It is worthwhile to note that the composition at the grain boundaries of Nitinol 60 is about 62 wt%, which corresponds to the composition of secondary phase Ni_4Ti_3 . As shown in Ref. [35], about 11% of Ni_4Ti_3 shows up at the grain boundaries of Nitinol 60, which verifies the simulation results to some extent.

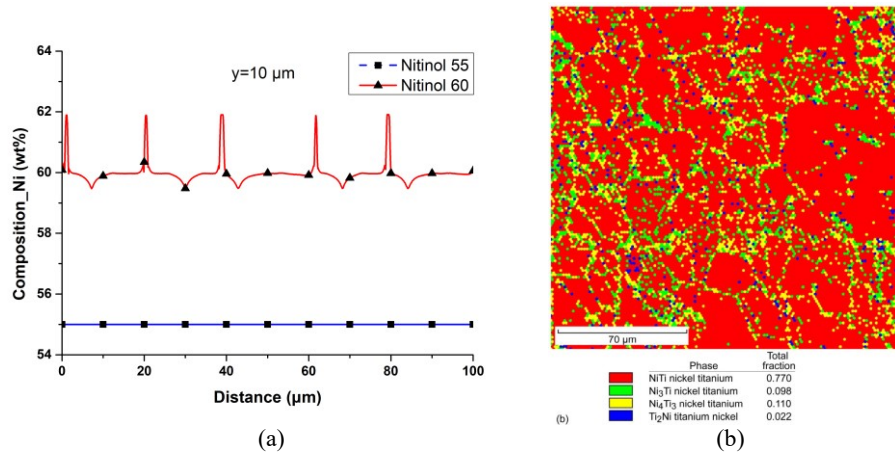


Figure 8. Solute distribution of Ni (a) Comparison of Nitinol 55 and Nitinol 60 at the location $y = 10 \mu\text{m}$ at 3 ms in simulation, (b) Experimental observation of phase distribution in Nitinol 60 produced by high temperature proprietary powder metallurgy process. Courtesy of Corte et al. [35].

1.4 FEA Simulation of Thermal Distribution and Fluid Flow in Melt Pool

The microstructures and properties of build parts are highly correlated with the geometry and dynamics of the melt pool. The simulation of the melt pool during the DED process is an important tool to develop a better understanding of the characteristics and mechanisms of the process. Furthermore, it is helpful for the optimization and control of process parameters [37]. Many researchers have been involved with simulation and analysis of the DED process including models of the powder stream process, models of the melt pool and models of microstructure, stress and final geometry [38]. For powder stream modeling, Tabernero et al. [39] simulated the powder flux distribution on a coaxial nozzle. A powder flow model was developed to predict the powder distribution shape,

particle velocities and trajectories. Zhu et al. [40] used a 2D discrete phase model of the gas-powder flow to compute the powder flow field distribution. For melt pool modeling, simplified heat transfer models were built to simulate the thermal history in earlier work [51, 52]. Hoadley and Rappaz [43] used a thermal model to demonstrate the linear relationship among the laser power, processing velocity, and the thickness of the deposited layer. Zhu et al. [44] analyzed the effect of curvature change on temperature distribution when building thin-walled rings. More complex models were also built by accounting for latent heat in the phase transformation [45], convection at the evolving interface [46], and fluid flow [47]. To predict the free surface evolution between liquid and gas phases, the level set method was also introduced [47–49]. Wen and Shin [51] adopted the level set method to predict the free surface and extended the thermal and fluid flow models to include the mass source term in the continuity equation and additional source terms of enthalpy and momentum due to the moving interface. Lee and Farson [52] analyzed the correlations between material parameters and fluid flow patterns and showed that the hemispherical melt pool free surface has different shaping mechanisms from the laser weld melt pool formed on the flat surface. Temperature profile is also helpful to investigate the microstructure affected by the processing parameters [52–54], and residual stresses [56]. Costa et al. [57] developed a thermo-kinetic finite element model to show the microstructural transformations and hardness variations in the deposition process. Toyserkani et al. [58] developed a thermal model to predict the dependency of the final geometry on the laser pulse shaping. The final geometry can also be affected by processing parameters [59] and the thermal stress and strain field [70, 71].

In addition to the DED process, SLM is a popular way to process alloys, which uses a high power-density laser to melt and fuse metallic powders on a pre-placed powder bed. Khairallah et al. [61, 62] explained the importance of including the stochastic nature of the powder bed. Furthermore they showed that the powder has lower thermal conductivity than bulk stainless steel, because the particles are at point contact and heat diffusion in gaps strongly depends on the thermal conductivity of the gas. Shen and Chou [64] explored the effect of powder porosity on the melt pool size and found that temperatures in the melt pool become higher with increasing porosity. The simulation with the thermal model can be used to analyze the size of the melt pool [65] and the effect of laser intensity, preheating temperature, and laser beam spot size on the temperature distribution [65–68]. The thermal model has been further coupled with the mechanical model to predict the stress field [69–71] and the distortion of the part [73]. Similar to simulations of the DED process, models of latent heat of fusion and fluid flow are important for simulating the liquid-solid interface in the SLM process [74]. Shiomi et al. [75] considered the latent heat and shrinkage due to solidification in the process and found that the amount of solidified parts and the maximum temperature of powders are significantly affected by the peak laser power. Gürtler et al. [76] used the multiphysics model to describe melting, wetting and solidification phenomena.

The effects of the powder-layer thickness, moving heat source intensity, scan spacing and scanning velocity on the process dynamics are shown. Dai and Shaw [87, 88] considered the effect of the powder-to-solid transition and investigated the transient temperature, transient stress and residual stress fields. It is also demonstrated that the volume shrinkage because of the transformation from a powder compact to dense liquid has a negligible effect on the temperature pattern [79].

In this study, FEA is used to discretize equations of thermal distributions and fluid flows, and COMSOL Multiphysics is used to model the melt pool in the DED process. Heat transfer, phase change, and fluid flow in the melt pool are included in the physics model. Some material properties used in the model are obtained from MD simulations. The geometry, temperature distribution and velocity field of the melt pool are analyzed. Temperatures and the velocity field are used in the phase field simulation.

1.4.1 Model Construction

In the DED process, the substrate is stationary and powder particles melted by the laser beam are deposited to a narrow and focused region on the substrate. The laser beam is assumed to move with a constant velocity and power level. The melt pool is formed within a small area under the laser beam, and the melt particles are solidified quickly given the high cooling rate. The movement of the laser beam creates a track of solidified material. The computational domain is set to be 9 mm \times 12 mm \times 6 mm as shown in Figure 9 (a). The laser beam is initially at location (0, 0, 6) and then moves along the positive y -direction. Only a half of the domain is modeled to reduce the computational cost with the symmetry assumption.

1.4.1.1 Continuum models

The evolution of the melt pool during a short time period is analyzed. The effect of the free surface between liquid and gas phases is negligible. The liquid-solid domain is characterized as pure solid, pure liquid and a mixture of solid and liquid (mushy zone). The density, thermal conductivity, and viscosity of the mushy zone can be defined respectively as

$$\rho_m = f_s \rho_s + f_l \rho_l \quad (3)$$

$$k_m = f_s k_s + f_l k_l \quad (4)$$

$$\mu_m = \mu_l \frac{\rho_m}{\rho_l} \quad (5)$$

where ρ_s and k_s are density and thermal conductivity in solid phase, and ρ_l and k_l are those in liquid phase, respectively. μ_l is the dynamic viscosity in the liquid phase. f_s and f_l are the solid and liquid mass fractions, which can be expressed as

$$f_l = \begin{cases} 1 & T > T_l \\ \frac{T-T_s}{T_l-T_s} & T_s \leq T \leq T_l \\ 0 & T < T_s \end{cases} \quad (6)$$

$$f_s = 1 - f_l \quad (7)$$

where T_s and T_l are solidus and liquidus temperatures, respectively. Some material properties of molten Nitinol 60 alloy are difficult to measure directly. The rule of mixtures

$$M_{\text{Nitinol}} = \omega_{Ni}M_{Ni} + \omega_{Ti}M_{Ti} \quad (8)$$

is applied, where M_{Ni} and M_{Ti} are material properties of Nickel and Titanium respectively, ω_{Ni} and ω_{Ti} are weight fractions of Nickel and Titanium respectively, and M_{Nitinol} is the corresponding material property of Nitinol alloy. The material properties of solid Nitinol 60 can be found in Table 1. The properties of molten Nickel, Titanium, and Nitinol 60 alloy are listed in Table 2.

Table 2. Material properties of molten Nickel, Titanium and Nitinol alloy [80]–[86].

Material properties	Pure Nickel	Pure Titanium	Nitinol alloy
Surface tension gradient ($\text{mJ m}^{-2} \text{K}^{-1}$)	-0.33	-0.27	-0.306
Surface tension (N m^{-1})	1.588	1.6264	1.6034
Viscosity (mPa s)	4.859	1.37	3.4634
Density (g cm^{-3})	7.85	4.106	6.3524
Thermal conductivity ($\text{W m}^{-1} \text{K}^{-1}$)	69	28	52.6
Thermal expansion (K^{-1})	5.49×10^{-5}	5.2024×10^{-5}	5.3750×10^{-5}
Specific heat capacity ($\text{J kg}^{-1} \text{K}^{-1}$)	735	790	757

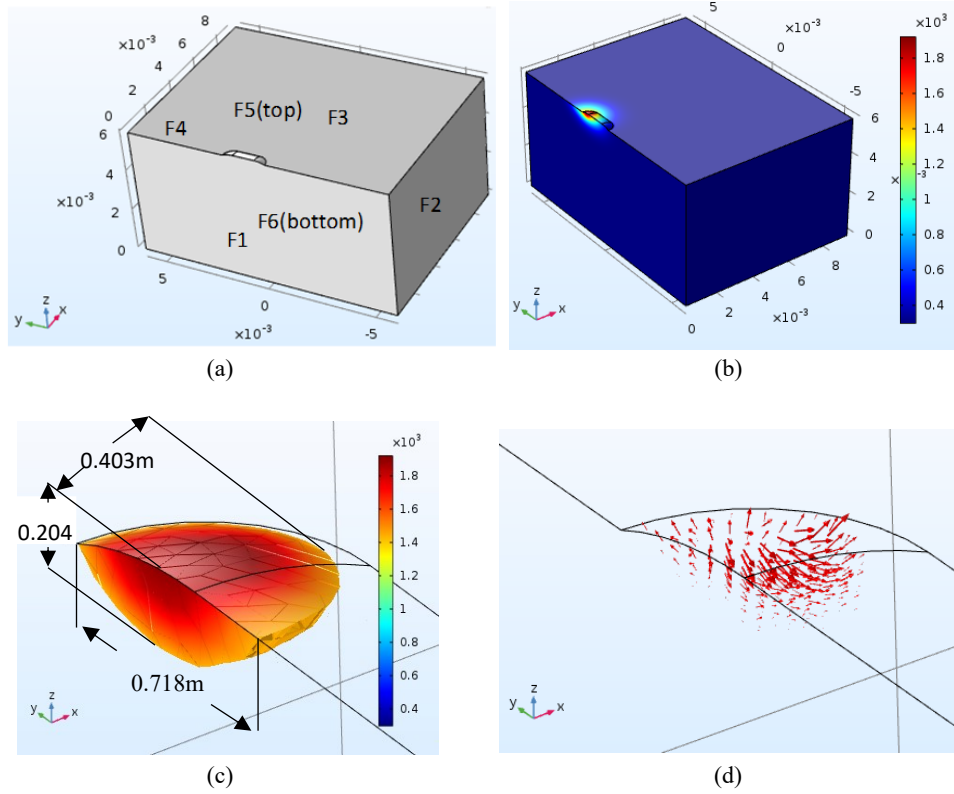


Figure 9. FEA model of temperature distribution, phase change, and fluid flow of the melt pool. (a) The computational domain, (b) Temperature distribution of the computational domain, (c) Temperature distribution and geometry of the melt pool at 41 ms, (d) The velocity field in the melt pool at 41 ms.

1.4.1.2 Heat transfer

Conservation of energy in the solid-liquid domain can be written as

$$\frac{\partial(\rho_m C_{pm} T)}{\partial t} + \vec{u} \cdot \nabla(\rho_m C_{pm} T) - k_m \nabla^2 T - \dot{S} = 0 \quad (9)$$

where T is the temperature, \vec{u} is the velocity field, and \dot{S} is the source term. Since there is a phase change in the modeling process, the apparent heat capacity method is used by including the latent heat as an additional term in the heat capacity. The effective heat capacity can be expressed as

$$C_{pm} = \frac{1}{\rho_m} (f_s \rho_s C_{ps} + f_l \rho_l C_{pl}) + L \frac{\partial \alpha_m}{\partial T} \quad (10)$$

where L is the latent heat and

$$\alpha_m = \frac{1}{2} \frac{f_s \rho_s - f_l \rho_l}{f_l \rho_l + f_s \rho_s}. \quad (11)$$

A set of boundary conditions should be satisfied for the heat transfer model. Boundary conditions on the top face F5 in Figure 9 (a) include heat flux from the laser source, convection, and radiation, which can be represented as

$$q''_{in_top} = q''_{LS} - h(T - T_0) - \sigma \varepsilon (T^4 - T_0^4) \quad (12)$$

where h is the heat transfer coefficient, T_0 is the ambient temperature, and σ and ε represent the Stefan-Boltzmann constant and the emissivity respectively. The laser source is assumed to be Gaussian distributed, as

$$q''_{LS} = \frac{2P\eta}{\pi R_L^2} \exp\left(-\frac{2r^2}{R_L^2}\right) \quad (13)$$

where P is the laser power, η is the laser absorbability, r is the radial distance to the center of the laser spot, and R_L is the effective laser beam radius.

Since only half of the domain is used, the symmetric boundary condition is applied on the front face F1. Other faces F2-F4 and F6 are assumed to be adiabatic.

1.4.1.3 Fluid flow

The fluid flow in this model is assumed to be incompressible and laminar flow. The conservation of mass is therefore formulated as

$$\nabla \cdot \vec{u} = 0 \quad (14)$$

and the conservation of momentum is

$$\rho_m \frac{\partial \vec{u}}{\partial t} + \rho_m (\vec{u} \cdot \nabla) \vec{u} = \nabla \cdot [-p + \vec{u}(\nabla \vec{u} + (\nabla \vec{u})^T)] + \vec{F}_b + \vec{F}_D \quad (15)$$

where p is the pressure, and \vec{F}_b is the buoyancy force due to the difference of the density in the melt pool and expressed as

$$\vec{F}_b = \rho_r \vec{g} [1 - \beta(T - T_r)] \quad (16)$$

where ρ_r and T_r are reference density and temperature, respectively, \vec{g} is the gravity field, and β is the thermal expansion coefficient. \vec{F}_D is a Darcy term representing the damping force when fluid passes through a porous medium and is formulated as

$$\vec{F}_D = -\frac{\mu_m}{K} \vec{u} \quad (17)$$

where K is the isotropic permeability and can be expressed as

$$K^{-1} = \frac{K_0^{-1}(1-f_l)^2}{f_l^3 + \tau} \quad (18)$$

where K_0 is a constant determined by the morphology of the mushy zone, and τ is a small number to avoid the singularity. For the pure solid, K approaches zero. For the pure liquid, K approaches to infinity.

A set of boundary conditions should be satisfied for the fluid flow model. On the top face F5, the capillary force is given by

$$\sigma_n = -\gamma \hat{n} \kappa \quad (19)$$

and Marangoni forces is given by

$$\sigma_t = \frac{d\gamma}{dT} \nabla_s T \quad (20)$$

where γ is the surface tension, \hat{n} is the normal direction, κ is the face curvature, and ∇_s is the gradient in the tangent plane. The capillary force acts in the normal direction, whereas the Marangoni force acts in the direction tangent to the surface. Symmetric boundary conditions are applied on the front face F1. Boundary conditions on other faces are assumed to be zero velocity.

1.4.2 Results and Discussion

The melt particles solidify quickly due to the high cooling rate, and the solid track is formed after the laser moves away. The heat absorbed by the melt pool dissipates into the environment and the substrate. Here, the geometry of a single track is predefined. The height and width of the single track on the top face F5 are assumed to be 0.1 mm and 0.48 mm. The laser spot moves along the positive y -direction with a velocity of 13 mm/s. The power of the laser is 800 W, and the radius of the laser beam is 1.25 mm. The laser absorptivity is 0.4 [87]. The initial temperature is assumed to be 300 K, and the initial velocity is 0 m/s.

The finite element method is used to discretize equations in heat transfer and fluid flow models. The mesh grid of the region near the laser beam is locally refined to ensure accurate computational results. The minimum element size of the mesh grid is set to be 1.48 μm . The segregated approach is used to solve the coupled models iteratively. That is, the heat transfer model and fluid flow model are solved sequentially until convergence. This method requires less memory than the fully coupled approach, where two physics models are solved simultaneously. The adaptive time stepping is used and the maximum time step is 0.1 ms to improve the convergence of results. It is found that the velocity result converges much slower than the temperature because the fluid flow model is highly nonlinear. The

melt pool is simulated for a short time period. The temperature and the size of the melt pool increase in this period. The melt pool is formed at 25 ms when the temperature of the substrate reaches the melting temperature. Figure 9 (b) shows the temperature field at 41 ms when the peak temperature is 1926 K. The geometry of the melt pool can be determined by setting the temperature range above the solidus temperatures. The length in the y -direction, height in the z -direction and width in the x -direction of the melt pool are 0.718 mm, 0.204 mm, and 0.403 mm respectively, as seen in Figure 9 (c). The velocity field is shown in Figure 9 (d), where the maximum velocity is 1.6 m/s. The fluid within the melt pool flows outward from the center due to the Marangoni force, which indicates the large gradient of the temperature on the surface. It is consistent with other findings that Marangoni force caused by the surface tension is dominant, whereas the buoyancy force is insignificant in the velocity field. Simulated results from the proposed model can be verified with results provided by Qi et al. [49] in terms of the peak temperature and velocity magnitudes, and the geometry of the melt pool. The detailed values may vary for different materials. The direct measurement of the temperature and velocity fields in melt pools is difficult, which makes the experimental validation a challenge.

The results from the FEA simulation can provide information to analyze the formation and evolution of the melt pool. The temperature and velocity fields can be further integrated with the phase field simulation to investigate the melting or solidification process in future work. To further improve the model, the level-set approach will be included to model the evolution of the liquid-gas interface.

1.5 Controlled Kinetic Monte Carlo as the Reduced-Order Model of DED Process

Simulation-based process optimization is the ultimate goal for process modeling, where the effective P-S-P relationship is established and the process parameters are optimized. This may require thousands of sampling points, each of which is a simulation run. Given that the simulations of high-fidelity FEA or PFM are computationally expensive, reduced-order models will be a more viable approach for process optimization. Here, cKMC modeling is proposed to simulate DED process at mesoscale. cKMC [88, 89] is a generalization of kinetic Monte Carlo (KMC). In KMC simulation, system state changes are triggered by random events. Therefore, KMC is not capable of simulating complete manufacturing processes that include external force or energy that deterministically affect system state changes. cKMC can solve these issues by including controlled events and controlled species. Controlled events and controlled species allow us to introduce deterministic events by specifying process direction or starting time.

KMC has been widely used to study self-assembly processes such as chemical vapor deposition and film growth. For instance, Zhu et al. [90] studied

the growth of NiTi alloy thin films using KMC. The roles of diffusion, substrate temperature, and deposition rate on forming the microstructures were studied. However, KMC is not able to simulate laser effects in the DED process. There has been some attempts on simulating AM processes with models similar to KMC. Rodgers et al. [91] studied grain growth in metal additive manufacturing using a Potts model. Grain microstructure evolution in the heat affected zone was simulated. Note that Potts model is also known as Ising model and does not capture the time of physical systems as KMC. Song et al. [92] used cKMC to simulate the laser-enhanced nanoparticle deposition process, where laser effect and film porosity were studied.

In this study, cKMC is used as a reduced-order model. Instead of the details in melting and solidification, cKMC models the fusion of Ni and Ti powders, and the geometry and porosity of the build. Each particle in cKMC is at the scale of powder. Particles are deposited on a lattice, fusion and diffusion occur during heating-cooling cycles and the geometry of part is formed. With the computational efficiency, process-structure relationships such as the one between laser power level and porosity can be established easily. Therefore, process parameters can be optimized to achieve the desirable deposition morphology and conversion rate of NiTi prior to experimentation.

1.5.1 Methodology

1.5.1.1 cKMC model setup

Figure 10 (a) shows the schematic diagram of the DED process, where Ni and Ti powders are injected, melted, fused into NiTi, and solidified. Here, x is the build direction and y is the hatch direction. The cKMC model size is $20 \times 20 \times 20$ lattice units and consists of 30,400 particles. The bottom of the simulation domain is the substrate, and the top contains Ni and Ti sources which are blended with Ni and Ti powders. Ni and Ti sources are powders that are being injected above the substrate. They are deposited sequentially corresponding to the scanning path. Therefore, they are defined as different species and named as *source11*, *source12*, *source13*, *source21*, *source22*, *source23*, etc. as shown in Figure 10 (b). The first notation means the layer number, and the second notation means the order of deposition within the layer. These sources are deposited one by one in a group. In this model, 6 groups of sources are used and the deposition sequence is 11, 12, 13, 21, 22, and 23. In the model, 12 different types of species are defined in total, as *Ni_source*, *Ni_active*, *Ni_liquid*, *Ni_solid*, *Ti_source*, *Ti_active*, *Ti_liquid*, *Ti_solid*, *NiTi_liquid*, *NiTi_solid*, *substrate*, *vacuum/void*. After the initial setup, the system evolves with events. Events for deposition, fusion, diffusion, activation, reheat, and solidification are defined in the following subsections.

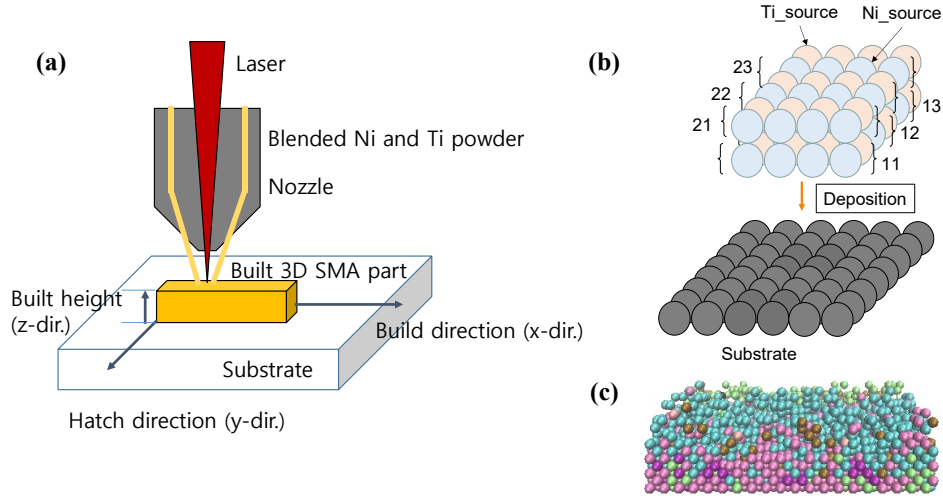


Figure 10. cKMC model of DED process. (a) Schematic diagram of DED process, (b) Initial setup where particles represent powder scale geometry, (c) A snapshot of cKMC model where different species are denoted by different colors

1.5.1.2 Events

Events in cKMC are divided into two types. One is stochastic, and the other is deterministic. Stochastic events are random events, and deterministic events are events that are affected by the external force or energy. The external energy in this process is the laser irradiation, and the external force is due to the air pressure. Stochastic events are defined in the same way as the normal events in KMC. Deterministic events are defined with controlled events and controlled species. Controlled species are the species that start transitions or reactions only at deterministic time. Controlled events are those events that only occur in certain neighborhoods with a specific direction or location. In controlled species command:

```
control_species reactant rate product x y z init_time
```

(x, y, z) specifies the direction or sequence that the reactant is converted to product, and init_time specifies when the conversion starts. In controlled events command:

```
control_event reactant1 reactant2 rate product1 product2 dx dy dz theta
```

(dx, dy, dz) specifies the direction in which the first and second reactants should be aligned. Theta is an angular allowance such that the direction formed by the

first and second reactants can be within the range of $\pm \theta$, where the reaction still occurs. The details of cKMC formalism can be found in Ref. [89].

In the DED process model, the regular events, controlled species, and controlled events are defined and listed in Table 3. Events (1) to (7) are defined for Ni. Similar events are also defined for Ti. The events of activation, deposition, fusion, diffusion, and solidification are illustrated in Figure 11. When multiple layers are deposited, the previously deposited layer will be reheated and some of the solid state material can become liquid state again. In this case, reheating events (9)-(11) will occur. The reheated Ni, Ti, and NiTi will be involved in the fusion and diffusion processes again. The events in multiple layer deposition are illustrated in Figure 12.

Table 3. Major events defined in DED process model.

Index	Events	Comments
(1)	$\text{Ni_src} \rightarrow \text{Ni_activated}$ (controlled species)"	activation
(2)	$\text{Ni_activated} + \text{vacuum} \rightarrow \text{vacuum} + \text{Ni_activated}$ (controlled events)	deposition
(3)	$\text{Ni_activated} + \text{substrate} \rightarrow \text{Ni_liquid} + \text{substrate}$ (controlled events)	deposition
(4)	$\text{Ni_activated} + \text{Ni_liquid} \rightarrow \text{Ni_liquid} + \text{Ni_liquid}$ (controlled events)	deposition
(5)	$\text{Ni_liquid} + \text{Ti_liquid} \rightarrow \text{NiTi_liquid} + \text{NiTi_liquid}$	fusion
(6)	$\text{Ni_liquid} + \text{void} + \text{substrate} \rightarrow \text{void} + \text{Ni_liquid} + \text{substrate}$	diffusion
(7)	$\text{Ni_liquid} \rightarrow \text{Ni_solid}$ (controlled species)	solidification
(8)	$\text{NiTi_liquid} \rightarrow \text{NiTi_solid}$ (controlled species)	solidification
(9)	$\text{Ni_solid} \rightarrow \text{Ni_liquid}$ (controlled species)	reheat
(10)	$\text{Ti_solid} \rightarrow \text{Ti_liquid}$ (controlled species)	reheat
(11)	$\text{NiTi_solid} \rightarrow \text{NiTi_liquid}$ (controlled species)	reheat

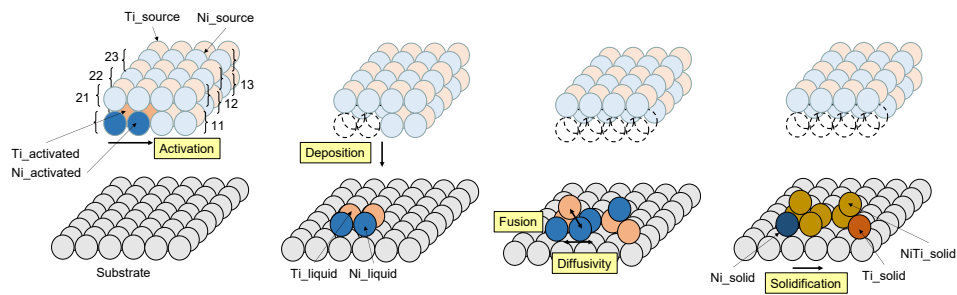


Figure 11. Examples of events for single layer deposition

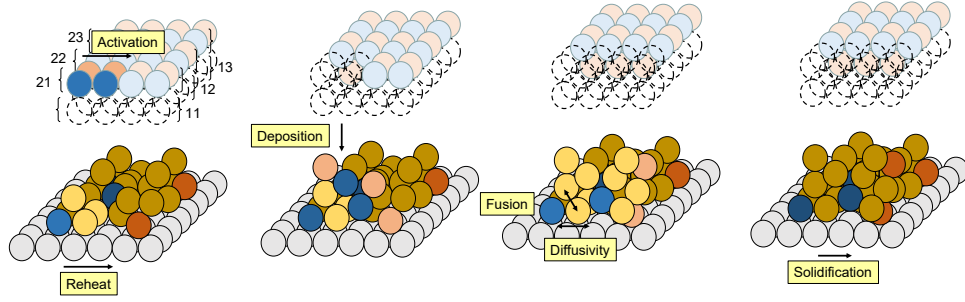


Figure 12. Examples of events for multiple-layer deposition

1.5.1.3 Calibration of rates

For each event, there is an associated rate. The values of rates are calibrated with sensitivity analysis. The rates involved in the modeled process are associated with deposition, fusion, diffusion, activation, reheat, and solidification. Activation and reheat rates are related to the laser scan speed. These rates can have a common effect on the simulation results such as conversion rate and porosity. Conversion rate is how much Ni and Ti is converted to NiTi. It is calculated by dividing the total number of NiTi particles at the final time step by the number of Ni and Ti powders at the first time step. Porosity is the ratio of void space to the volume of the built part, calculated from the number of solidified Ni, Ti, and NiTi particles divided by the total sites in the 3D part. For simplicity, sensitivity analysis is done on the diffusion rate while keeping other rates fixed. The results of sensitivity analysis are shown in Figure 13. The calibration is done according to the values of porosity in Ref. [91].

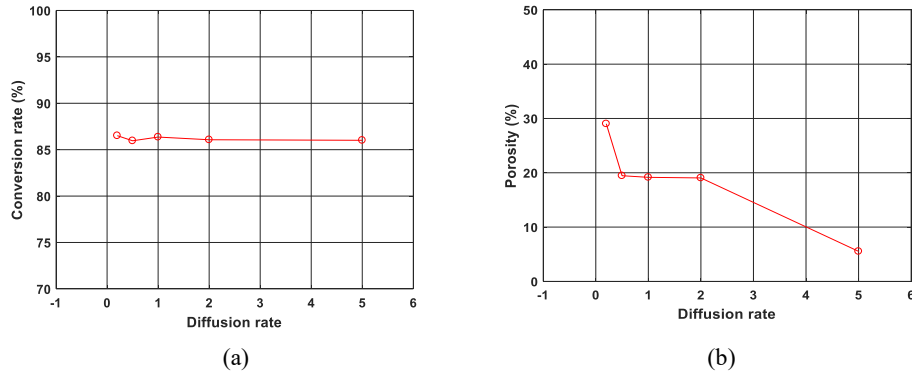


Figure 13. Sensitivity analysis of diffusion rate with respect to (a) conversion rate and (b) porosity

1.5.2 Results and Discussions

Laser condition is one of the most important factors that decide the quality of build in the DED process. After the model parameter calibration, the conversion rate and porosity of the NiTi were analyzed with different laser scan speeds and power levels. Results are shown in Figure 14, which shows that higher laser power leads to slightly higher conversion rate. The conversion rates show the values between 85% and 90%. Conversion rate is more related to laser power than laser scan speed.

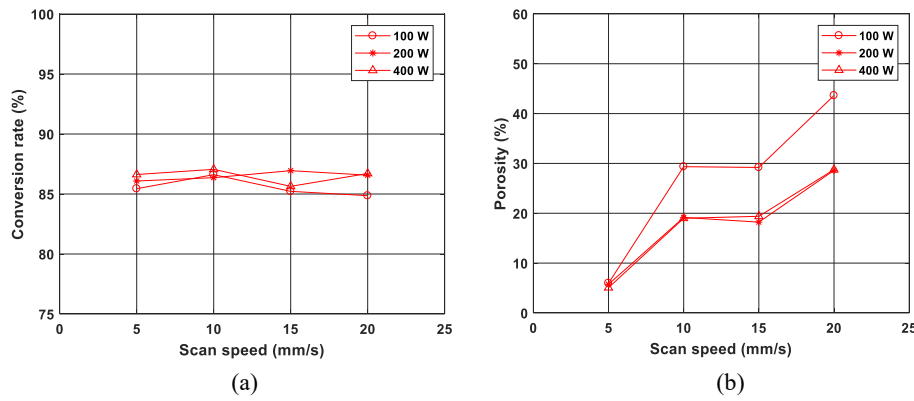


Figure 14. Predicted effects of laser power and scanning speed. (a) Conversion rate with different laser scan speed and power, (b) Porosity with different laser scan speed and power.

Porosity increases with higher laser scan speed, especially with low laser power. In addition, laser condition of higher laser power results in lower porosity. The porosity of the structure varies from 5% to 45% depending on the different laser and deposition conditions. If the laser power is higher, the melting of powders can be more complete. There is a higher chance that the solid-state particles transform to the liquid state and moves around to fill the void space within the structure. The diffusion of the materials in the liquid state will be more effective. As a result, a denser structure is built. On the other hand, if the laser power level is low, there is less possibility for the solid state to completely liquefy and diffuse. Therefore, a structure with high porosity will be formed. However, there is no significant difference in porosity values between the laser conditions of 200 W and 400 W, compared to those of 100 W and 200 W, as shown in Figure 14(b). There is a power level threshold for the materials to reach the melting point. A laser power level that is higher than the threshold will result in energy inefficiency or damage on the substrate. In addition, the scan speed also affects the porosity of the NiTi structure. If the scan speed is high, there is less time for the powder to fully absorb the laser energy. Therefore, porous structures will be generated. A low

scanning speed gives enough time for laser energy to be transferred to the powders, and denser structures can be built. In particular, with the low scan speed of 5 mm/s, there is no difference in the porosity values among the different laser conditions. We can conclude that porosity is related to the amount of heat transferred to the powder within a time unit. Higher laser power and slower scan speed will result in lower porosity. The simulation results show a good agreement with the experimental results reported by other researchers. For example, Bimber et al. [93] showed that the values of porosity of the NiTi alloy fabricated by the DED process was between 7% and 33%, depending on the process conditions. In addition, Krishna et al. [94] reported that the porosity of NiTi alloy samples was 12% to 36% when the laser power was 150 W to 200 W and the scan speed was 10 mm/s to 20 mm/s. The value of recovered deformation, which is related to the conversion rate in the cKMC model, was also ranging from 75% to 100%.

Pores and defects formed during the DED process affect the properties and performance of the shape memory alloy. Therefore, it is important to select the process parameters that create dense structures with high-purity NiTi. The proposed reduced-order model can be used to construct the process-structure relationship efficiently for process optimization.

1.6 Summary

ICME simulation tools can accelerate the materials and process design. In this study, a multiscale modeling framework that integrates MD, PF-TLBM, FEA, and cKMC mechanisms was used to examine the DED process of Nitinol. The multiscale modeling techniques enable the predictions of the material structures and properties at different length and timescales, which provides the insight into the effects of Nitinol composition on material properties and process parameters on microstructures and morphology of the final build. MD at the atomic scale provides the predictions of material properties such as melting temperature and lattice thermal conductivity for different compositions of SMAs. These properties are important factors to be considered when device and processes are designed. Purely relying on experimental studies to decide material properties is time consuming.

Time scale is the major concern in simulating manufacturing processes. MD has difficulty simulating manufacturing processes such as solidification and machining. It is only appropriate for ultrafast processes at the scale of nanoseconds (e.g. nanoscale sintering [95]). Mesoscale simulations are needed to build process-structure relationships. Here a new PF-TLBM scheme for solidification and grain growth at mesoscale is demonstrated, where liquid-to-solid phase transition and the effects of thermal gradient and liquid flow are revealed. These external factors are directly related to process parameters such as laser power and scanning speed. It is shown that the composition of Nitinol has a significant influence on the grain growth patterns during solidification, and on the final phase distribution. The

impact of process parameters on the dendritic growth and grain structures needs to be investigated thoroughly in order to establish the accurate process-structure relationship. Given the computational complexity of phase field simulation, larger scale simulations such as FEA are still valuable, even though material-related information cannot be predicted by them. Here, FEA is used to examine the geometry and dynamics of the melt pool by combining heat transfer, phase transition, and fluid flow models. The size and geometry of the melt pool and fluid velocity field can be predicted. High-fidelity PFM or FEA simulations are too expensive for extensive sampling in order to elucidate full P-S-P relationships and process optimization. Reduced-order modeling is a more viable approach. Here, a cKMC model is demonstrated to predict porosity and morphology of the build from different laser power levels and scanning speeds. It was shown that high laser power and slow scan speed help form a dense structure with reasonable conversion rate. This reduced-order model can reduce computational time from hours or days for FEA and PFM simulations to minutes for cKMC. Together, these multiscale modeling techniques enable a detailed study of the P-S-P relationships for additively manufactured Nitinol. Information exchange between these simulation tools is necessary for a comprehensive simulation-based process optimization framework. These methods are generic and can also be applied to investigate other materials and additive manufacturing systems.

Each of the individual simulation methods employed in this study provided some unique insight into the process-structure or structure-property relationships of Nitinol. However, to establish the complete P-S-P relationships, the integration of multiple modeling techniques is critical. Given the nature of information exchange between these models, the full integration requires that the simulations be synchronized while the input-output information update between them continue concurrently. A full automation can be computationally challenge in either a standalone or a distributed environment. The complexity of integrated simulation increases when more complex and detailed process models are introduced, e.g. including more physics, heterogeneous material models, and dynamic or adaptive process planning. In addition, these simulation techniques require significant initial development time to prepare and verify the simulation methods. The calibration and validation of these models themselves can be a daunting task. Once models are ready to predict, the requirement of generating massive amounts of data to examine the P-S-P relationships can be computationally prohibitive, because of the curse-of-dimensionality issue where many process parameters and factors need to be considered. When developing the models and examining the results, the developer also must ensure that the predictions are robust and accurate by carefully considering and quantifying uncertainty associated with these models. This is important to ensure validity of the simulation predictions.

In future work, these multiscale modeling techniques can be further enhanced to avoid some of the limitations of the current approaches. The models currently use certain assumptions to reduce computational complexity, which can

hinder the accuracy and robustness of prediction. Each model balances the tradeoffs of fidelity to computational efficiency and can be adjusted to capture more information. For instance, the MD models can be expanded to coarse grained models that allow for the calculation of properties that require a longer simulation time period. More sensitivity analysis needs to be done for the PF-TLBM simulations. It has been shown that the PFM predictions are sensitive to the settings of process parameters and material properties [96]. More physical information can also be added into the PFM, FEA, and cKMC simulations for an improved accuracy while balancing the computational time for different physical phenomena. Physical phenomena or events can potentially be combined if strong correlations can be identified, which can reduce the computational draw during the computation of the models. Currently several simulations utilize experimentally-obtained properties. The availabilities of these properties can be limited because of the capabilities in experiment observations for small length scales or short time scales. Model calibration and validation can be generalized with the calculated properties from *ab initio* simulations. Information assimilation between simulations and experiments can overcome the limitations in experiments in order to generate accurate simulation models. For instance, the interatomic potentials in MD models can be calibrated from both density functional theory calculations and experimental observations. MD can be used to predict more physical properties required for PFM, FEA, and cKMC simulations.

Acknowledgements

This research was supported in part by the National Science Foundation with grants IGERT-1258425 and CMMI-1306996, and the Basic Research Lab Program through the National Research Foundation of Korea funded by the MSIT (2018R1A4A1059976).

References

- [1] R. Rahmanian, N. Shayesteh Moghaddam, C. Haberland, D. Dean, M. Miller, and M. Elahinia, "Load bearing and stiffness tailored NiTi implants produced by additive manufacturing: a simulation study," vol. 905814, no. March 2014, p. 905814, 2014.
- [2] S. Shiva, I. A. Palani, S. K. Mishra, C. P. Paul, and L. M. Kukreja, "Investigations on the influence of composition in the development of Ni-Ti shape memory alloy using laser based additive manufacturing," *Opt. Laser Technol.*, vol. 69, no. 1, pp. 44–51, 2015.
- [3] M. H. Elahinia, M. Hashemi, M. Tabesh, and S. B. Bhaduri, "Manufacturing and processing of NiTi implants: A review," *Prog. Mater.*

- Sci.*, vol. 57, no. 5, pp. 911–946, 2012.
- [4] M. Elahinia, N. Shayesteh Moghaddam, M. Taheri Andani, A. Amerinatanzi, B. A. Bimber, and R. F. Hamilton, “Fabrication of NiTi through additive manufacturing: A review,” *Prog. Mater. Sci.*, vol. 83, pp. 630–663, 2016.
 - [5] X. Wang *et al.*, “Topological design and additive manufacturing of porous metals for bone scaffolds and orthopaedic implants: A review,” *Biomaterials*, vol. 83, pp. 127–141, 2016.
 - [6] C. Haberland, M. Elahinia, J. M. Walker, H. Meier, and J. Frenzel, “On the development of high quality NiTi shape memory and pseudoelastic parts by additive manufacturing,” *Smart Mater. Struct.*, vol. 23, no. 10, 2014.
 - [7] S. Saedi, A. S. Turabi, M. T. Andani, C. Haberland, H. Karaca, and M. Elahinia, “The influence of heat treatment on the thermomechanical response of Ni-rich NiTi alloys manufactured by selective laser melting,” *J. Alloys Compd.*, vol. 677, pp. 204–210, 2016.
 - [8] B. V. Krishna, S. Bose, and A. Bandyopadhyay, “Fabrication of porous NiTi shape memory alloy structures using laser engineered net shaping,” *J. Biomed. Mater. Res. - Part B Appl. Biomater.*, vol. 89, no. 2, pp. 481–490, 2009.
 - [9] M. Taheri Andani *et al.*, “Achieving biocompatible stiffness in NiTi through additive manufacturing,” *J. Intell. Mater. Syst. Struct.*, vol. 27, no. 19, pp. 2661–2671, 2016.
 - [10] Z.-Y. Zeng, C.-E. Hu, L.-C. Cai, X.-R. Chen, and F.-Q. Jing, “Molecular dynamics study of the melting curve of NiTi alloy under pressure,” *J. Appl. Phys.*, vol. 109, no. 4, pp. 043503-043503-6, Feb. 2011.
 - [11] P. Chowdhury, L. Patriarca, G. Ren, and H. Sehitoglu, “Molecular dynamics modeling of NiTi superelasticity in presence of nanoprecipitates,” *Int. J. Plast.*, vol. 81, pp. 152–167, Jun. 2016.
 - [12] Y. U. Wang, Y. M. Jin, and A. G. Khachaturyan, “The effects of free surfaces on martensite microstructures: 3D phase field microelasticity simulation study,” *Acta Mater.*, vol. 52, no. 4, pp. 1039–1050, Feb. 2004.
 - [13] H. M. Paranjape, S. Manchiraju, and P. M. Anderson, “A phase field – Finite element approach to model the interaction between phase transformations and plasticity in shape memory alloys,” *Int. J. Plast.*, vol. 80, pp. 1–18, May 2016.
 - [14] A. Baz and J. Ro, “Thermo-dynamic characteristics of nitinol-reinforced composite beams,” *Compos. Eng.*, vol. 2, no. 5–7, pp. 527–542, Jan. 1992.
 - [15] L. C. Brinson and R. Lammering, “Finite element analysis of the behavior of shape memory alloys and their applications,” *Int. J. Solids Struct.*, vol.

30, no. 23, pp. 3261–3280, Jan. 1993.

- [16] P. Entel *et al.*, “Fundamental Aspects of Magnetic Shape Memory Alloys: Insights from ab initio and Monte Carlo Studies,” 2010.
- [17] V. D. Buchelnikov *et al.*, “Monte Carlo study of the influence of antiferromagnetic exchange interactions on the phase transitions of ferromagnetic Ni-Mn- X alloys (X = In, Sn, Sb),” *Phys. Rev. B*, vol. 78, no. 18, p. 184427, Nov. 2008.
- [18] S. Yoo, X. C. Zeng, and S. S. Xantheas, “On the phase diagram of water with density functional theory potentials: The melting temperature of ice Ih with the Perdew–Burke–Ernzerhof and Becke–Lee–Yang–Parr functionals,” *J. Chem. Phys.*, vol. 130, no. 22, p. 221102, Jun. 2009.
- [19] S. Yoo, S. S. Xantheas, and X. C. Zeng, “The melting temperature of bulk silicon from ab initio molecular dynamics simulations,” *Chem. Phys. Lett.*, vol. 481, no. 1–3, pp. 88–90, Oct. 2009.
- [20] E. Schwegler, M. Sharma, F. Gygi, and G. Galli, “Melting of ice under pressure,” *Proc. Natl. Acad. Sci. U. S. A.*, vol. 105, no. 39, pp. 14779–83, Sep. 2008.
- [21] S. W. Watt, J. A. Chisholm, W. Jones, and S. Motherwell, “A molecular dynamics simulation of the melting points and glass transition temperatures of myo- and neo-inositol,” *J. Chem. Phys.*, vol. 121, no. 19, pp. 9565–9573, Nov. 2004.
- [22] J. R. Morris and X. Song, “The melting lines of model systems calculated from coexistence simulations.”
- [23] A. B. Belonoshko, R. Ahuja, and B. Johansson, “Quasi– *Ab Initio* Molecular Dynamic Study of Fe Melting,” *Phys. Rev. Lett.*, vol. 84, no. 16, pp. 3638–3641, Apr. 2000.
- [24] J. R. Morris, C. Z. Wang, K. M. Ho, and C. T. Chan, “Melting line of aluminum from simulations of coexisting phases,” *Phys. Rev. B*, vol. 49, no. 5, pp. 3109–3115, Feb. 1994.
- [25] T. Farrell and D. Greig, “The thermal conductivity of nickel and its alloys,” *J. Phys. C Solid State Phys.*, vol. 2, p. 1465, 1969.
- [26] S. Plimpton, “Modeling Thermal Transport and Viscosity with Molecular Dynamics Tackling a new problem with LAMMPS,” no. March, pp. 2014–2225, 2014.
- [27] X. Zheng, D. G. Cahill, P. Krasnochtchekov, R. S. Averback, and J.-C. Zhao, “High-throughput thermal conductivity measurements of nickel solid solutions and the applicability of the Wiedemann–Franz law,” *Acta Mater.*, vol. 55, no. 15, pp. 5177–5185, Sep. 2007.
- [28] M. W. Ackerman, K. Y. Wu, and C. Y. Ho, “Lattice Thermal Conductivity

- and Lorenz Function of Copper-Nickel and Silver-Palladium Alloy Systems,” in *Thermal Conductivity 14*, Boston, MA: Springer US, 1976, pp. 245–257.
- [29] M. G. Holland, “Analysis of Lattice Thermal Conductivity,” *Phys. Rev.*, vol. 132, no. 6, pp. 2461–2471, Dec. 1963.
- [30] I. Steinbach, “Phase-field models in materials science,” *Model. Simul. Mater. Sci. Eng.*, vol. 17, no. 7, p. 073001, 2009.
- [31] D. Liu and Y. Wang, “Mesoscale Multi-Physics Simulation of Solidification in Selective Laser Melting Process Using a Phase Field and Thermal Lattice Boltzmann Model,” in *Volume 1: 37th Computers and Information in Engineering Conference*, 2017, no. 58110, p. V001T02A027.
- [32] D. Liu and Y. Wang, “Mesoscale multi-physics simulation of rapid solidification of Ti-6Al-4V alloy,” *Addit. Manuf.*, vol. 25, pp. 551–562, Jan. 2019.
- [33] B. B. Laird, “The solid-liquid interfacial free energy of close-packed metals: Hard-spheres and the turnbull coefficient,” *J. Chem. Phys.*, vol. 115, no. 7, pp. 2887–2888, 2001.
- [34] P. Ternik and R. Rudolf, “Numerical analysis of continuous casting of niti shape memory alloy,” *Int. J. Simul. Model.*, vol. 15, no. 3, pp. 522–531, 2016.
- [35] C. Della Corte, S. V Pepper, R. Noebe, D. R. Hull, and G. Glennon, “Intermetallic Alloys for Bearing Applications,” *Power Transm. Eng.*, no. March 2009, 2009.
- [36] I. Loginova, G. Amberg, and J. Ågren, “Phase-field simulations of non-isothermal binary alloy solidification,” *Acta Mater.*, vol. 49, no. 4, pp. 573–581, 2001.
- [37] D. Hu and R. Kovacevic, “Sensing, modeling and control for laser-based additive manufacturing,” *Int. J. Mach. Tools Manuf.*, vol. 43, no. 1, pp. 51–60, Jan. 2003.
- [38] A. J. Pinkerton, “Advances in the modeling of laser direct metal deposition,” *J. Laser Appl.*, vol. 27, no. S1, p. S15001, Feb. 2015.
- [39] I. Tabernero, A. Lamikiz, E. Ukar, L. N. López de Lacalle, C. Angulo, and G. Urbikain, “Numerical simulation and experimental validation of powder flux distribution in coaxial laser cladding,” *J. Mater. Process. Technol.*, vol. 210, no. 15, pp. 2125–2134, Nov. 2010.
- [40] G. Zhu, D. Li, A. Zhang, and Y. Tang, “Numerical simulation of metallic powder flow in a coaxial nozzle in laser direct metal deposition,” *Opt. Laser Technol.*, vol. 43, no. 1, pp. 106–113, Feb. 2011.

- [41] P. Peyre, P. Aubry, R. Fabbro, R. Neveu, and A. Longuet, “Analytical and numerical modelling of the direct metal deposition laser process,” *J. Phys. D. Appl. Phys.*, vol. 41, no. 2, p. 025403, Jan. 2008.
- [42] S. Kumar, S. Roy, C. P. Paul, and A. K. Nath, “Three-Dimensional Conduction Heat Transfer Model for Laser Cladding Process,” *Numer. Heat Transf. Part B Fundam.*, vol. 53, no. 3, pp. 271–287, Jan. 2008.
- [43] A. F. A. Hoadley and M. Rappaz, “A thermal model of laser cladding by powder injection,” *Metall. Trans. B*, vol. 23, no. 5, pp. 631–642, Oct. 1992.
- [44] G. Zhu, A. Zhang, D. Li, Y. Tang, Z. Tong, and Q. Lu, “Numerical simulation of thermal behavior during laser direct metal deposition,” *Int. J. Adv. Manuf. Technol.*, vol. 55, no. 9–12, pp. 945–954, Aug. 2011.
- [45] C. Cho, G. Zhao, S.-Y. Kwak, and C. B. Kim, “Computational mechanics of laser cladding process,” *J. Mater. Process. Technol.*, vol. 153–154, pp. 494–500, Nov. 2004.
- [46] M. F. Gouge, J. C. Heigel, P. Michaleris, and T. A. Palmer, “Modeling forced convection in the thermal simulation of laser cladding processes,” *Int. J. Adv. Manuf. Technol.*, vol. 79, no. 1–4, pp. 307–320, Jul. 2015.
- [47] V. Manvatkar, A. De, and T. DebRoy, “Heat transfer and material flow during laser assisted multi-layer additive manufacturing,” *J. Appl. Phys.*, vol. 116, no. 12, p. 124905, Sep. 2014.
- [48] L. Han, K. M. Phatak, and F. W. Liou, “Modeling of laser cladding with powder injection,” *Metall. Mater. Trans. B*, vol. 35, no. 6, pp. 1139–1150, Dec. 2004.
- [49] H. Qi, J. Mazumder, and H. Ki, “Numerical simulation of heat transfer and fluid flow in coaxial laser cladding process for direct metal deposition,” *J. Appl. Phys.*, vol. 100, no. 2, p. 024903, Jul. 2006.
- [50] X. He and J. Mazumder, “Transport phenomena during direct metal deposition,” *J. Appl. Phys.*, vol. 101, no. 5, p. 053113, Mar. 2007.
- [51] S. Wen and Y. C. Shin, “Modeling of transport phenomena during the coaxial laser direct deposition process,” *J. Appl. Phys.*, vol. 108, no. 4, p. 044908, Aug. 2010.
- [52] Y. Lee and D. F. Farson, “Simulation of transport phenomena and melt pool shape for multiple layer additive manufacturing,” *J. Laser Appl.*, vol. 28, no. 1, p. 012006, Feb. 2016.
- [53] B. Zheng, Y. Zhou, J. E. Smugeresky, J. M. Schoenung, and E. J. Lavernia, “Thermal Behavior and Microstructure Evolution during Laser Deposition with Laser-Engineered Net Shaping: Part II. Experimental Investigation and Discussion,” *Metall. Mater. Trans. A*, vol. 39, no. 9, pp. 2237–2245, Sep. 2008.

- [54] T. Amine, J. W. Newkirk, and F. Liou, "An investigation of the effect of direct metal deposition parameters on the characteristics of the deposited layers," *Case Stud. Therm. Eng.*, vol. 3, pp. 21–34, Jul. 2014.
- [55] Y. Zhang, G. Yu, X. He, W. Ning, and C. Zheng, "Numerical and experimental investigation of multilayer SS410 thin wall built by laser direct metal deposition," *J. Mater. Process. Technol.*, vol. 212, no. 1, pp. 106–112, Jan. 2012.
- [56] S. Ghosh and J. Choi, "Three-dimensional transient finite element analysis for residual stresses in the laser aided direct metal/material deposition process," *J. Laser Appl.*, vol. 17, no. 3, pp. 144–158, Aug. 2005.
- [57] L. Costa, R. Vilar, T. Reti, and A. M. Deus, "Rapid tooling by laser powder deposition: Process simulation using finite element analysis," *Acta Mater.*, vol. 53, no. 14, pp. 3987–3999, Aug. 2005.
- [58] E. Toyserkani, A. Khajepour, and S. Corbin, "3-D finite element modeling of laser cladding by powder injection: effects of laser pulse shaping on the process," *Opt. Lasers Eng.*, vol. 41, no. 6, pp. 849–867, Jun. 2004.
- [59] H. El Cheikh, B. Courant, S. Branchu, J.-Y. Hascoët, and R. Guillén, "Analysis and prediction of single laser tracks geometrical characteristics in coaxial laser cladding process," *Opt. Lasers Eng.*, vol. 50, no. 3, pp. 413–422, Mar. 2012.
- [60] M. Alimardani, E. Toyserkani, and J. P. Huissoon, "A 3D dynamic numerical approach for temperature and thermal stress distributions in multilayer laser solid freeform fabrication process," *Opt. Lasers Eng.*, vol. 45, no. 12, pp. 1115–1130, Dec. 2007.
- [61] F. Brückner, D. Lepski, and E. Beyer, "Modeling the Influence of Process Parameters and Additional Heat Sources on Residual Stresses in Laser Cladding," *J. Therm. Spray Technol.*, vol. 16, no. 3, pp. 355–373, Aug. 2007.
- [62] S. A. Khairallah and A. T. Anderson, "Mesoscopic Simulation Model of Selective Laser Melting of Stainless Steel Powder," *J. Mater. Process. Technol.*, vol. 214, no. 11, pp. 2627–2636, 2014.
- [63] S. A. Khairallah, A. Anderson, A. M. Rubenchik, J. Florando, S. Wu, and H. Lowdermilk, "Simulation of the main physical processes in remote laser penetration with large laser spot size," *AIP Adv.*, vol. 5, no. 4, p. 047120, Apr. 2015.
- [64] N. Shen and K. Chou, "Thermal Modeling of Electron Beam Additive Manufacturing Process: Powder Sintering Effects," in *ASME 2012 International Manufacturing Science and Engineering Conference*, 2012, p. 287.

- [65] M. Jamshidinia, F. Kong, and R. Kovacevic, "Temperature Distribution and Fluid Flow Modeling of Electron Beam Melting® (EBM)," in *Volume 7: Fluids and Heat Transfer, Parts A, B, C, and D*, 2012, p. 3089.
- [66] G. Bugada Miguel Cervera and G. Lombera, "Numerical prediction of temperature and density distributions in selective laser sintering processes," *Rapid Prototyp. J.*, vol. 5, no. 1, pp. 21–26, Mar. 1999.
- [67] S. Kolossov, E. Boillat, R. Glardon, P. Fischer, and M. Locher, "3D FE simulation for temperature evolution in the selective laser sintering process," *Int. J. Mach. Tools Manuf.*, vol. 44, no. 2–3, pp. 117–123, 2004.
- [68] I. A. Roberts, C. J. Wang, R. Esterlein, M. Stanford, and D. J. Mynors, "A three-dimensional finite element analysis of the temperature field during laser melting of metal powders in additive layer manufacturing," *Int. J. Mach. Tools Manuf.*, vol. 49, no. 12–13, pp. 916–923, Oct. 2009.
- [69] L. Dong, A. Makradi, S. Ahzi, and Y. Remond, "Three-dimensional transient finite element analysis of the selective laser sintering process," *J. Mater. Process. Technol.*, vol. 209, no. 2, pp. 700–706, Jan. 2009.
- [70] M. Matsumoto, M. Shiomi, K. Osakada, and F. Abe, "Finite element analysis of single layer forming on metallic powder bed in rapid prototyping by selective laser processing," *Int. J. Mach. Tools Manuf.*, vol. 42, no. 1, pp. 61–67, Jan. 2002.
- [71] A. Hussein, L. Hao, C. Yan, and R. Everson, "Finite element simulation of the temperature and stress fields in single layers built without-support in selective laser melting," *Mater. Des.*, vol. 52, pp. 638–647, Dec. 2013.
- [72] D. Riedlbauer, P. Steinmann, and J. Mergheim, "Thermomechanical finite element simulations of selective electron beam melting processes: performance considerations," *Comput. Mech.*, vol. 54, no. 1, pp. 109–122, Jul. 2014.
- [73] K. Dai and L. Shaw, "Thermal and stress modeling of multi-material laser processing," *Acta Mater.*, vol. 49, no. 20, pp. 4171–4181, Dec. 2001.
- [74] J. F. Li, L. Li, and F. H. Stott, "A three-dimensional numerical model for a convection–diffusion phase change process during laser melting of ceramic materials," *Int. J. Heat Mass Transf.*, vol. 47, no. 25, pp. 5523–5539, Dec. 2004.
- [75] M. Shiomi, A. Yoshidome, F. Abe, and K. Osakada, "Finite element analysis of melting and solidifying processes in laser rapid prototyping of metallic powders," *Int. J. Mach. Tools Manuf.*, vol. 39, no. 2, pp. 237–252, Feb. 1999.
- [76] F.-J. Gürtler, M. Karg, K.-H. Leitz, and M. Schmidt, "Simulation of Laser Beam Melting of Steel Powders using the Three-Dimensional Volume of Fluid Method," *Phys. Procedia*, vol. 41, pp. 881–886, 2013.

- [77] K. Dai and L. Shaw, "Thermal and mechanical finite element modeling of laser forming from metal and ceramic powders," *Acta Mater.*, vol. 52, no. 1, pp. 69–80, Jan. 2004.
- [78] K. Dai and L. Shaw, "Parametric studies of multi-material laser densification," *Mater. Sci. Eng. A*, vol. 430, no. 1–2, pp. 221–229, Aug. 2006.
- [79] K. Dai and L. Shaw, "Finite element analysis of the effect of volume shrinkage during laser densification," *Acta Mater.*, vol. 53, no. 18, pp. 4743–4754, Oct. 2005.
- [80] J. Tille and J. C. Kelly, "The surface tension of liquid titanium," *Br. J. Appl. Phys.*, vol. 14, no. 10, pp. 717–719, Oct. 1963.
- [81] V. E. Zinoviev, "Thermal properties of metals at high temperatures," *A Handb.*, 1989.
- [82] H. M. L. and Q. Jiang*, "Surface Tension and Its Temperature Coefficient for Liquid Metals," 2005.
- [83] H. Wang, S. Yang, and B. Wei, "Density and structure of undercooled liquid titanium," *Chinese Sci. Bull.*, vol. 57, no. 7, pp. 719–723, Mar. 2012.
- [84] Engineering ToolBox, "Metals - as Liquids." [Online]. Available: https://www.engineeringtoolbox.com/liquid-metal-boiling-points-specific-heat-d_1893.html. [Accessed: 27-Jun-2018].
- [85] K. Zhou, H. P. Wang, J. Chang, and B. Wei, "Experimental study of surface tension, specific heat and thermal diffusivity of liquid and solid titanium," *Chem. Phys. Lett.*, vol. 639, pp. 105–108, Oct. 2015.
- [86] R. E. Rozas, A. D. Demirağ, P. G. Toledo, and J. Horbach, "Thermophysical properties of liquid Ni around the melting temperature from molecular dynamics simulation," *J. Chem. Phys.*, vol. 145, no. 6, p. 064515, Aug. 2016.
- [87] Z. Sparks, T. E., & Fan, "Measurement of laser absorption coefficient of several alloys for diode laser," *Unpubl. Rep.*, 2006.
- [88] Y. Wang, "Controlled Kinetic Monte Carlo Simulation of Nanomanufacturing Processes," in *Volume 2: 31st Computers and Information in Engineering Conference, Parts A and B*, 2011, pp. 241–252.
- [89] Y. Wang, "Controlled Kinetic Monte Carlo Simulation for Computer-Aided Nanomanufacturing," *J. Micro Nano-Manufacturing*, vol. 4, no. 1, p. 011001, Sep. 2015.
- [90] Y. Zhu and X. Pan, "Kinetic Monte Carlo simulation of 3-D growth of NiTi alloy thin films," *Appl. Surf. Sci.*, vol. 321, pp. 24–29, Dec. 2014.
- [91] T. M. Rodgers, J. D. Madison, and V. Tikare, "Simulation of metal additive

- manufacturing microstructures using kinetic Monte Carlo,” *Comput. Mater. Sci.*, vol. 135, pp. 78–89, Jul. 2017.
- [92] J.-H. Song, K.-H. Choi, R. Dai, J.-O. Choi, S.-H. Ahn, and Y. Wang, “Controlled kinetic Monte Carlo simulation of laser improved nano particle deposition process,” *Powder Technol.*, vol. 325, pp. 651–658, Feb. 2018.
- [93] B. A. Bimber, R. F. Hamilton, J. Keist, and T. A. Palmer, “Anisotropic microstructure and superelasticity of additive manufactured NiTi alloy bulk builds using laser directed energy deposition,” *Mater. Sci. Eng. A*, vol. 674, pp. 125–134, Sep. 2016.
- [94] B. V. Krishna, S. Bose, and A. Bandyopadhyay, “Fabrication of porous NiTi shape memory alloy structures using laser engineered net shaping,” *J. Biomed. Mater. Res. Part B Appl. Biomater.*, vol. 89B, no. 2, pp. 481–490, May 2009.
- [95] J. M. Sestito, F. Abdeljawad, T. A. L. Harris, Y. Wang, and A. Roach, “An atomistic simulation study of nanoscale sintering: The role of grain boundary misorientation,” *Comput. Mater. Sci.*, vol. 165, no. April, pp. 180–189, 2019.
- [96] A. Tran, D. Liu, H. Tran, and Y. Wang, “Quantifying uncertainty in the process-structure relationship for Al–Cu solidification,” *Model. Simul. Mater. Sci. Eng.*, vol. 27, no. 6, p. 064005, Sep. 2019.